Numerical Modeling of the Ladle Flow by a LES-Based Eulerian–Lagrange Approach: A Systematic Survey

TIM HAAS, CHRISTIAN SCHUBERT, MORITZ EICKHOFF, and HERBERT PFEIFER

To account for increasing economic and ecological pressure, the steel industry is obligated to continuously optimize all processes. An important optimization approach is numerical modeling although its potential is limited by the accuracy of the mathematical models. In a previous work, a validation database was created and a validation score was derived from this data which allows a comprehensive qualitative accuracy assessment for those models. Here, this system is employed for a systematic optimization of the isothermal flow in the casting ladle. For that, different submodels, namely the turbulence models, subgrid turbulence models, bubble-induced turbulence and interfacial closure models as well as influencing factors, such as the grid resolution or the initial bubble size, are analyzed. It is shown that the large eddy turbulence model is more accurate than the Reynolds-average approach because it is able to reproduce the anisotropy of turbulence in the bubble region. In accordance with the literature, a grid dependency of the lift force is found which can be reduced using an averaged shear field as an additional variable. For the interfacial closure models, the combination of the Tomiyama drag model for fully contaminated systems and the Tomiyama lift correlation showed the best agreement with the experimental data. The results of the survey are summarized to a best-practice guideline with which the validation score can be increased from 38.7 with the Reynolds-average approach to 85.1 on a coarse grid respectively, and 87.8 on a fine grid. However, some upscaling problems of the numerical system from the water model to the real ladle are revealed. There is a need to find accurate yet efficient grid resolutions which make the large eddy turbulence model affordable with the current computational resources. Furthermore, alloying elements or non-metallic inclusions might alter the interfacial forces considerably. However, no studies on their effect have been published yet.

I. INTRODUCTION

THE casting ladle is one of the most important aggregates in secondary steel metallurgy. It is used for transportation, charging and homogenization of alloying elements. Additionally, a homogeneous casting temperature is adjusted and non-metallic inclusions can be removed. However, the demands on the process control are growing constantly. Customers are demanding steadily decreasing final contents of non-metallic inclusions. Shorter process times and low energy consumption must be guaranteed from an economic point of view and environmental aspects are becoming increasingly important in society.

Therefore, a continuous optimization of the plants and process control is necessary. In principle, there are three different strategies for this: plant trials, physical simulations and numerical modeling. For all three, important measurements or models are summarized in the overviews by Mazumdar and Guthrie[1] and more recently by Liu et al.[2]

Plant trials are carried out directly in the process and thus enable a dedicated improvement of specific problems. On the other hand, they are purely empirical and it is very difficult to measure certain variables. Furthermore, they are expensive and time-consuming. Therefore, the improvement by means of plant trials usually takes place in very small increments.

The second possibility are physical models. Usually, geometrically downscaled water models are used. These are comparatively cheap and allow direct access to many measured variables. On the other hand, the scalability of

TIM HAAS, CHRISTIAN SCHUBERT, MORITZ EICKHOFF, and HERBERT PFEIFER are with the Department for Industrial Furnaces and Heat Engineering, RWTH Aachen University, Kopernikusstraûe 10, 52074 Aachen, Germany. Contact e-mail: haas@iob.rwth-aachen.de

the results remains a problem especially for multiphase flows. Therefore, not all phenomena can be modeled accurately.

Thirdly, there is the possibility of numerical modeling. This method is also cheap and allows direct access to a large number of influencing variables. On the other hand, reality is represented by a mathematical model which often greatly simplifies the complexity of the overall system. In addition, correlations are unknown or cannot be precisely described mathematically, yet. This is particularly the case with multiphase flows. These accuracy limitations restrict the optimization potential of numerical simulation. By reviewing the latest numerical models, it becomes evident that research concentrated on the development or refinement of metallurgy-related submodels like inclusion removal or mixing, not on the basic flow though it determines the prediction accuracy of the model and all subsystems. Especially due to the nowadays necessary detailed improvement, a considerable uncertainty remains by optimization with numerical modeling. This uncertainty makes a comprehensive validation mandatory. However, almost all published works on the flow in the ladle furnace have found at least "reasonable', but mostly 'good' or even 'excellent' agreement between the model and validation data. That is somewhat surprising since the employed models have enormously evolved in complexity. Because of this discrepancy, different validation methods were critically reviewed.[3] It was shown that flow measurements are a good and sensitive validation method. However, the presentation as a line plot can lead to misleading results, because a lot of information is lost, for example the flow direction or the flow structure. A contour plot with vectors is a good validation method, but it requires a plot for every investigated model and allows only a qualitative comparison. In addition, it might not be sensitive enough to analyze bubble-related submodels. Flow measurements in the multiphase region are also a well suited method. However, it is primarily used to validate submodels of the bubble column model and does not necessarily allow conclusions about the flow in the rest of the ladle. Similar considerations apply to the analysis of the bubble rising velocity. The analysis of the slag eye is not sensitive enough. 'Good' results could be obtained with all numerical models, even if they sometimes generated very different flow fields. Finally, a validation with the mixing time was investigated. This method is sensitive enough to investigate the suitability of the whole model, but not to compare different submodels. However, a major issue is that the mixing time measurements themselves are subject to a large measurement uncertainty. On the basis of these investigations it was concluded that for a complete, sensitive validation, flow measurements inside and outside the multiphase region as well as an analysis of the bubble column in the water model should be performed. The final optimized numerical model of the water model experiment can then be scaled to the industrial ladle. The scaling should then be validated again with mixing time measurements.

To create a starting point for a sensitive and standardized validation procedure, a database[4] for the isothermal flow in a water model was recently created in cooperation with international computational fluid dynamics (CFD) experts. The database includes high speed measurements of the bubble column as well as flow measurements using particle image velocimetry (PIV) in the single-phase and multiphase area and an uncertainty analysis of the measurement techniques. From this data a scoring system was derived which measures the accuracy of the numerical model by a single number.[5] Thereby a value of 100 indicates that all predicted values meet the measured ones within the uncertainty range. This score allows a systematic analysis and a quantified optimization of the numerical models. A major advantage of this method is that it allow a complete quantitative validation with a single, instead of evaluating the plots for the flow field, the flow in the bubble column and the bubble rising velocity individually. The overall score is composed of various subscores that reveal additional optimization potentials:

Toroid (Max. score: 10): The 'toroid' subscore compares the predicted and measured position of the point where the radial flow near the surface is redirected into a downward axial flow. Thereby the prediction accuracy of the general flow structure and the position of possible dead zones is assessed.

Means (Max. score: 20): The 'means' subscore compares the numerically calculated mean values of the velocity components and their fluctuation with the measured values on the plane of symmetry. This evaluates the extent to which the numerical model predicts the strength of the flow and thus is able to predict mixing, refractory wear or removal of inclusions.

Monitors (Max. score: 40): The 'monitors' subscore is a refinement of the previous subscores. Here the flow direction and the velocity components, as well as their fluctuation are compared at eight defined control points on the plane of symmetry as well as on the plane perpendicular to it. Thereby conclusions can be drawn about the prediction accuracy of the flow structure and the flow velocity.

Bubbles (Max. score: 15): The 'bubble' subscore compares the calculated and measured mean bubble rising velocity and the width of the bubble plume at five different heights. It allows a detailed optimization of all bubble-related submodels that play a major role in the formation of the flow as well as heat and mass transfer in the ladle.

Plume (Max. score: 15) The 'plume' subscore evaluates the prediction accuracy of the numerical model with respect to the axial velocity and the width of the flow profile of the continuous phase in the plume region. Similar to the bubble subscore it allows an optimization of all bubble-related submodels.

The different maximum scores result in a weighting of the individual subsystems. This was done empirically, considering the importance of the different subsystems for the overall accuracy of the numerical model. This weighting represents a first draft and could possibly be adjusted in the future, based on feedback from other researchers.

To increase the optimization potential by means of numerical simulation, a structured analysis of multiphase models for the isothermal flow in a water model of a 185 t ladle is carried out in this work. Based on the scoring system, the influence of different submodels is investigated and current research results from mesoscale

systems are transferred to the macroscale problem of the ladle. The analysis involves turbulence modeling, grid resolution, subgrid scale turbulence modeling, bubble-induced turbulence (BIT), interfacial closure models and the influence of the bubble size. The results of that survey are summarized to a best-practice guideline for the modeling of the flow in the ladle and upscaling challenges are revealed and discussed.

II. INITIAL NUMERICAL MODEL

First, the initial numerical model is described. Note that throughout this work, some parameters are adjusted based on the results of the different submodel studies.

The investigated system is a 1:5 water model of a 185 t steel ladle, shown in Figure 1. A more detailed description of the geometry can be found in Reference 5. The geometry is slightly simplified. The bottom is assumed to be straight, not curved as in the physical model. The effect of this simplification is discussed later. A no-slip boundary condition is applied to all walls, the opening is modeled by a wall with a no-shear condition.

For the computations, a structured hexahedral grid is created. The skewness of the cells is reduced by an O-grid with a radius of 0.2 m at the center of the model. The influence of the average cell size on the solution is investigated throughout this work.

A gas flow rate of 2.4 slm is investigated which ensures dynamic similarity with an industrial argon flow rate of 134 L/min based on the plume Froude number criterion proposed by Krishnapisharody and Irons.[6] In
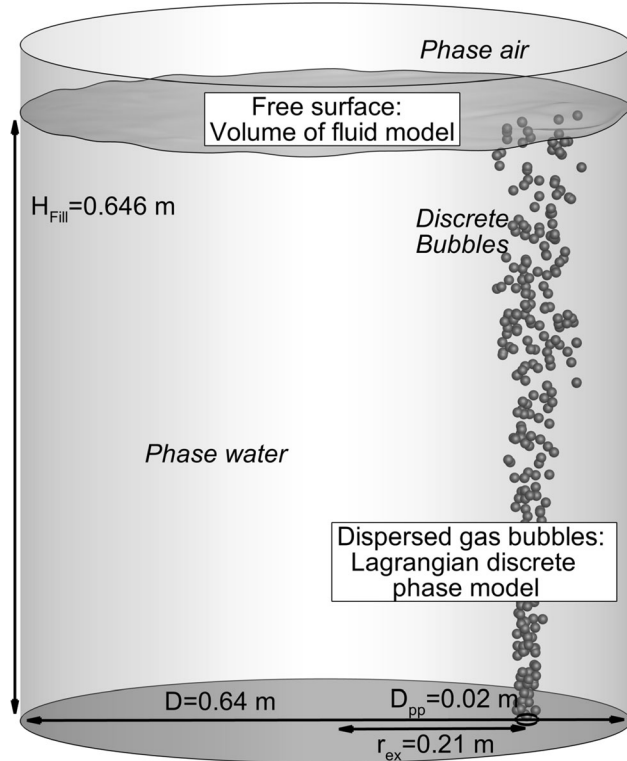

Figure 1—Dimensions, phases and modeling strategies for the water model of a 185 t ladle.

line with the validation database, fluid properties at a temperature of 20 °C are employed which are listed in Table I.

As indicated in Figure 1, the system comprises two continuous phases and one dispersed phase which requires two different multiphase approaches. The continuous phases, air and water, are modeled with the Eulerian approach. Their phase boundary, that is to say the top bath level, is calculated with the Volume of Fluid (VOF) interface tracking method.[7] Thereby, the volume fraction F_n of each phase is computed by

$$\frac{\partial F_n}{\partial t} + \frac{\partial}{\partial x_i}(F_n \vec{u}_i) = 0 \qquad [1]$$

Since there are only two continuous phases, Eq. [1] is merely solved for the secondary phase. The volume fraction of the primary phase is calculated by the restriction, that a cell must not have empty space. Values between 0 and 1 indicate the existence of a phase boundary. The normal direction of the phase boundary points in the direction in which the value of F_n changes most rapidly. The physical properties employed in the set of conservation equations are calculated by weighting the properties of the phases by their volume fraction F_n. In cells that contain a phase boundary, the effect of surface tension is modeled by an additional source term in the momentum equations. The conservation equations for the continuous phases are discretized by the non-diffusive bounded central difference scheme.

For the modeling of the dispersed gas phase, the Eulerian–Lagrange approach (E–L) is chosen. It provides information on the position of discrete bubbles, but no complete spatial or temporal resolution of all flow structures in the direct vicinity of the bubble is made. Thereby, the trajectories of the bubbles are computed by a force balance:

$$\frac{\partial \vec{u}_B}{\partial t} = \frac{1}{m_B}\sum_i \vec{F}_{B,i} \qquad [2]$$

where $\vec{u}_B$ is the bubble velocity, m_B is the bubble mass and $\vec{F}_{B,i}$ are mass-based forces on the bubble. The bubble position $\vec{x}_B$ is computed by

$$\frac{\partial \vec{x}_B}{\partial t} = \vec{u}_B \qquad [3]$$

Table I. Employed Physical Properties

Parameter	Unit	Value
Phase Water		
Density	kg/m^3	998.2
Viscosity	Pa s	0.001003
Surface Tension	N/m	0.07275
Phase Air		
Density	kg/m^3	1.225
Viscosity	Pa s	1.789×10^{-5}
Dispersed Gas Bubbles		
Density at Injection	kg/m^3	1.279

The bubble's trajectories are computed by a coupled solution of Eqs. [2] and [3]. These ordinary differential equations are approximated by a 5th order Runge–Kutta scheme.

For momentum exchange, a two-way coupling between the discrete phase and the continuous phases is applied. The impact of the bubbles on the continuous phase is modeled by adding an additional source term in the momentum equations:

$$\vec{F}_{ex} = \vec{F}_i \dot{m}_B \Delta t \qquad [4]$$

To reduce the grid dependency of two-way coupling, the source term is averaged over the nodes of the cell in which the bubble is located in

$$\overline{\vec{F}_{ex}} = \vec{F}_{ex} \frac{\frac{1}{|\vec{x}_B - \vec{x}_n|}}{\sum_i \frac{1}{|\vec{x}_B - \vec{x}_n|}} \qquad [5]$$

where $\vec{x}_n$ is the location of the nodes.

A. *Bubble Force Balance*

Bubbles are released with an equivalent diameter of 4.25 mm into the computational domain, which is in line with the data provided in the validation database. The effect of the bubble size and the size distribution is discussed throughout this work. On their rising path, the bubbles grow slightly because of a declining static pressure according to

$$d_B(z) = d_{B,0} \left(\frac{\rho_F g H_{Fill} + p_0}{\rho_F g (H_{Fill} - z) + p_0} \right)^{1/3} \qquad [6]$$

where $d_{B,0}$ is the initial equivalent diameter, H is the bath height, z is the current bubble height, p_0 is the atmospheric pressure and ρ_F is the fluid density. All bubbles are removed from computation as they reach the phase boundary which is indicated by an air volume fraction F_n above 0.1.

As Eq. [2] states, the trajectories are determined by the forces acting on the bubble. These forces arise mainly from local pressure gradients along the bubble surface. However, as the close vicinity of the bubbles is not resolved, semi-empiric interfacial closure models are employed. In this work, the buoyancy force, drag force, lift force and virtual mass force are modeled. The closures are expressed in dependency of the dimensionless bubble Reynolds and Eotvos number:

$$Re_B = \frac{\rho_F |\vec{u}_B - \vec{u}_F| d_B}{\mu_F} \qquad [7]$$

$$Eo = \frac{g(\rho_F - \rho_B) d_B^2}{\sigma}, \qquad [8]$$

where $\vec{u}_F$ is the fluid velocity, μ_F is the fluid viscosity and σ is the surface tension between bubble and fluid.

Although many different correlations have been established over the years, the non-drag forces in particular are not fully understood yet and cannot be comprehensively modeled mathematically. Thus, the effect of different correlations is discussed throughout this work. Here, only the models employed in the initial numerical models are described. The drag force determines the bubble rising velocity and is the main contribution to the exchanged momentum between bubbles and fluid. It is given by

$$\vec{F}_D = C_D \frac{\pi d_B^2}{4} \frac{\rho_F}{2} (\vec{u}_B - \vec{u}_F)^2 \qquad [9]$$

Equation [9] indicates that the drag force is directly proportional to the dimensionless drag coefficient C_D, which depends on bubble properties and the flow conditions. Numerous attempts to determine C_D are available. Tomiyama et al.[8] reviewed existing measurements and derived different drag correlation for three different degrees of contamination. In this work, the equation for fully contaminated systems is utilized, since for the experiments in the database non-purified tab water was used and PIV tracers were added:

$$C_D = \max \left[\frac{24}{Re_B} \left(1 + 0.15 Re_B^{0.687} \right), \frac{8}{3} \frac{Eo}{Eo + 4} \right] \qquad [10]$$

The lift force is important for the lateral spreading of the plume. In this work, the equation for a shear induced lift force[9] is employed:

$$\vec{F}_L = C_L \frac{\pi d_B^2}{6} \rho_F (\vec{u}_B - \vec{u}_F) \times \nabla \vec{u}_F, \qquad [11]$$

where $\nabla \vec{u}_F$ indicates the shear field by the spatial derivatives of the fluid flow vector. For the lift coefficient C_L the approximation by Tomiyama et al.,[10] slightly modified by Frank et al.,[11] is used. The correlation gives credit to the rising importance of the unsteady wake with increasing bubble diameter by a change of signs of C_L:

$$C_L = \begin{cases} \min[0.288 \tanh(0.121 Re_B; f(Eo_d)] & Eo_d \leq 4 \\ f(Eo_d) & 4 < Eo_d \leq 10 \\ -0.27 & Eo_d > 10 \end{cases} \qquad [12]$$

$$f(Eo_d) = 0.00105 Eo_d^3 - 0.0159 Eo_d^2 + 0.474 \qquad [13]$$

Eo_d is the modified Eotvos number which considers the deformation of larger bubbles into ellipsoids rather than spheroids:

$$Eo_d = \frac{g(\rho_F - \rho_B) d_h^2}{\sigma} \qquad [14]$$

where d_h is the length of the major axis of the deformed bubble. To estimate the deformation,

Tomiyama et al.[10] proposed to use the correlation by Wellek et al.[12]:

$$d_h = d_B(1 + 0.163Eo^{0.757})^{1/3} \qquad [15]$$

The virtual mass force arises from the acceleration of the surrounding fluid caused by the acceleration of the bubble:

$$\vec{F}_{VM} = C_{VM} \frac{\rho_F}{\rho_B} \left(\vec{u}_B \nabla \vec{u}_F - \frac{d\vec{u}_B}{dt} \right) \qquad [16]$$

The virtual mass coefficient C_{VM} is assumed 0.5 in this work.

B. Solution Procedure

The time step size is set to 0.005 seconds so that the Courant–Friedrichs–Lewy (CFL) number is well below one for all mesh resolutions:

$$CFL = \frac{\Delta t u_{max}}{\Delta x_{min}} < 1 \qquad [17]$$

In case the large eddy simulation turbulence model (LES) is used, which does not calculate an averaged flow field but the instantaneous flow, the flow has to be averaged sufficiently long. In all calculations presented, calculations are carried out for 180 seconds where the first 60 seconds are not included in the averaging procedure. In the last 10.9 seconds, following the guidelines of the validation database, an additional analysis of the gas bubbles is carried out. With this averaging period, the residual uncertainty of the mean value is less than 1 pct. The simulations are carried out using Fluent 2019 R3.

III. INFLUENCE OF DIFFERENT SUBMODELS

A. Turbulence Model

The modeling of turbulence is one of the most important aspects of CFD. Thus, its influence on the isothermal flow in the ladle is investigated. Due to the limitation of the computer capacity, it is not possible to resolve the smallest temporal and spatial scales of turbulence in most industrial applications. Instead, an additional modeling approach has to be employed. In the past decades, this has usually been the statistical Reynolds-averaged Navier–Stokes (RANS) approach. Here, the flow is not resolved in time, but the mean flow field and mean flow fluctuations are calculated. The turbulence is considered by the Boussinesq eddy viscosity hypothesis, that is to say by an increment of the viscosity by an artificial turbulent viscosity. The LES model presents an alternative approach which becomes more attractive when the computing capacity is increased using computing clusters. Here, a relatively fine computational grid is used and all turbulence scales larger than the numerical grid (supergrid scales) are modeled directly by solving the Navier–Stokes equations. For all finer scales (subgrid scales), a subgrid model similar to the RANS approach is used.

In this work, the RANS standard k–ε model is compared to the LES model with the dynamic Smagorinsky subgrid model (Eq. [A1]). Apart from the turbulence model, the two models are identical and employ the submodels described above. The calculations are performed on a grid with an average cell width of 6 mm. The scores of the two systems are shown in Figure 2.

The analysis reveals that the LES model (score: 79.9) represents the validation data much better than the RANS model (score: 38.7). The main reason for the difference between the models can be found in the plume region. As shown by the different velocity fluctuation components in the validation database,[4] the Boussinesq assumption of isotropic turbulence does not apply in this region. While the fluctuation components are almost equal in the single-phase region, the fluctuation in axial direction distinctly exceeds the fluctuation in radial direction in the plume region. While that cannot be considered by the RANS approach, it can be modeled on the supergrid scale with the LES model. Hence, the LES model is superior to RANS models in systems with anisotropic turbulences like the ladle and is further investigated in the following. Though LES provides information about the instantaneous flow and higher accuracies, it also comes along with some model-specific challenges, summarized in a review by Dhotre et al.[13] These challenges will be addresses in the subsequent sections. By a more detailed analysis of the comparison of the turbulence models, it is possible to identify the main factors that limit the scoring of the LES model. As shown in the diagram, the toroid position is predicted almost perfectly. The mean velocity and velocity fluctuation of the x-component of velocity is predicted within the measurement uncertainty which means a maximum scoring, while both values are slightly overpredicted for the z-component. The monitoring scoring is somewhat lower which is mainly due to the fact that this score is stricter than the monitoring score in regards of the scoring range and the measurement uncertainty. This is particularly the case for the velocity fluctuations. All monitoring points yield similar scores. However, point 6 ($x = 150$ mm, $y = 0$, $z = 500$ mm) which is the monitor closest to the plume has the lowest score. In general, it can be concluded that the single-phase region is very well predicted with the LES turbulence model. The subsystems related to the plume region, bubbles and plume, show that the numerical model overpredicts both the liquid as well as the bubble velocity, while it underpredicts the width of the profiles. These subsystems show the largest optimization potential.

Apart from the model-specific challenges, it was noted in preliminary studies that coupled E–L LES calculations with Fluent can differ strongly from each other despite the use of identical models and settings. These differences went far beyond the residual error and could reach up to 15 pct for certain monitoring points. This observation was made with different grid resolutions, time steps, solver settings, geometries, computation systems, parallelization strategies and Fluent versions. Therefore, the variation of the validation score is compared in three calculations with the same settings
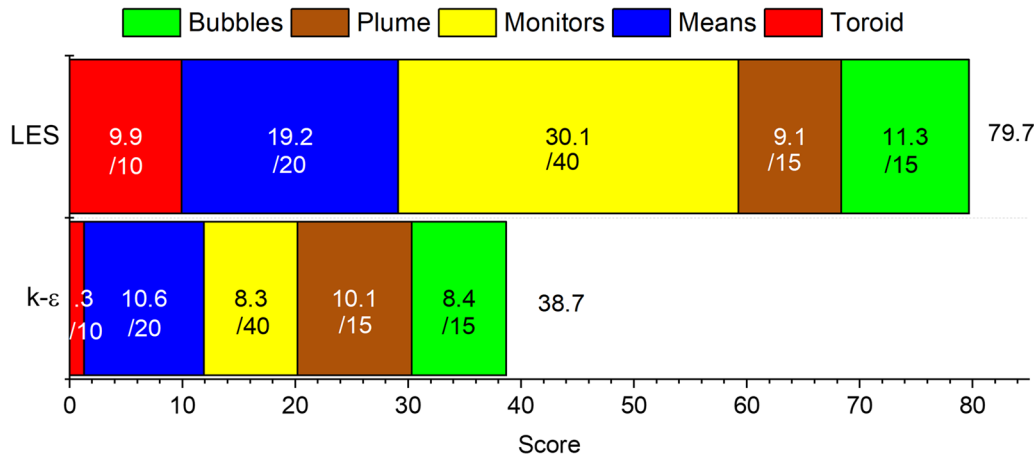
Figure 2—Scores of the different turbulence models.

in the preliminary LES studies. It is found that the spread of the total validation score is in the range of 0.5. However, for different monitoring points, the differences could still be found.

B. Subgrid Model

While the LES model computes supergrid turbulences directly, the effect of smaller turbulence scales is estimated by models based on the Boussinesq hypothesis. The reason behind it is that smaller scales tend to be more isotropic than larger ones. For the increase of the viscosity by the subgrid scale turbulent viscosity μ_t, the mixing-length concept by Smagorinsky[14] and the turbulent kinetic energy transport model by Deardorff[15] are tested.

A comparison of the two models was carried out for the E–E model by Niceno et al.[16] where the subgrid model of turbulent kinetic energy transport showed slightly better predictions of the turbulent kinetic energy. More importantly, this model allows a consideration of bubble-induced turbulences as an additional source term in Eq. (A3), which significantly improved the prediction of the velocity fluctuations. For the E–L model Sungkorn et al.[17] investigated the influence of the Smagorinsky constant and found little effect on the solution, especially when the constant exceeded 0.1. A comparison of the different subgrid turbulence models for E–L is not known to the authors.

The scores of the different subgrid turbulence models are given in Figure 3. It reveals that the choice of the subgrid model does not affect the accuracy of the overall numerical model much. The subgrid turbulent kinetic energy model yield slightly lower scorings, mainly because the toroid is predicted too centric and the overprediction of the velocity components is increased slightly.

A more detailed analysis of the results can be made by comparing the time-averaged axial velocity fluctuation in the plume region at a height of 0.36 m, shown in Figure 4. A distinction is made between the resolved

part of the supergrid scales and the modeled part using the subgrid model. The fluctuation components have to be computed in different ways as described in the appendix.

It can be seen from Figure 4, that both models reproduce the double peak of w' which is characteristic for bubble columns. However, only the dynamic Smagorinsky model is able to reproduce the asymmetry caused by different flow conditions on the sides of the plume. Both models overestimate the axial velocity fluctuation, though the overestimate is more pronounced in the subgrid turbulent kinetic energy transport model.

C. Grid Resolution

The grid resolution influences the numerical solution in different ways. The numerical error depends on the cell width Δx which also defines the filter size for implicit LES, i.e., the turbulence fraction which is calculated directly and which is approximated by a subgrid model. While these two factors aim for the finest possible grid resolution, an opposite effect was observed for multiphase models. As an ideal tradeoff, Milelli et al.[18] established the following criterion for the Eulerian–Eulerian (E–E) model:

$$1.2 < \frac{\Delta x}{d_B} < 1.5 \qquad [18]$$

However, this criterion does not apply as strictly to the Lagrange as to the Eulerian approach, since the model is based on different assumptions. Moreover, mapping techniques[19–21] were developed to further reduce the grid dependency. Still, existing studies investigating the effect of the grid size on E–L LES models were carried out in a range similar to the Milelli criterion. Sungkorn et al.[17] examined three different grid resolutions for a bubble column with a bubble size d_B of 4 mm, $\Delta x/d_B = 1.5$ ($\Delta x = 6$ mm), 1.25 ($\Delta x = 5$ mm), and 1.1 ($\Delta x = 4.4$ mm). It was found that the coarsest grid resolution leads to a too narrow
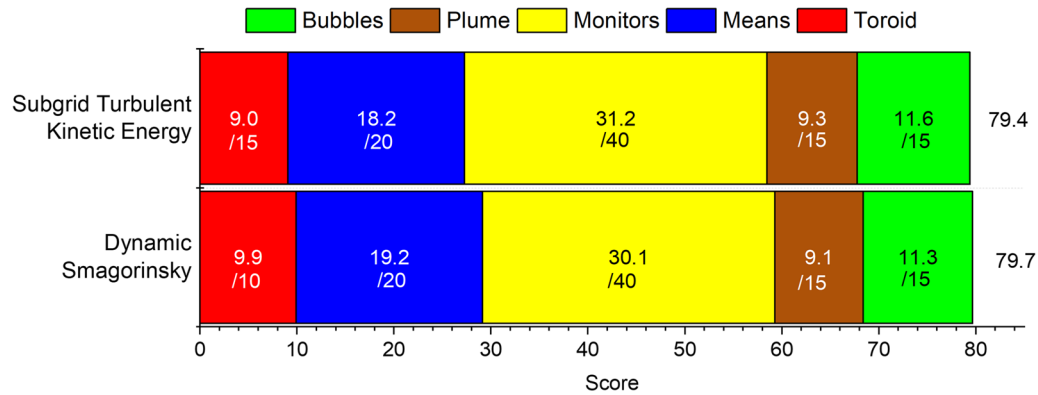
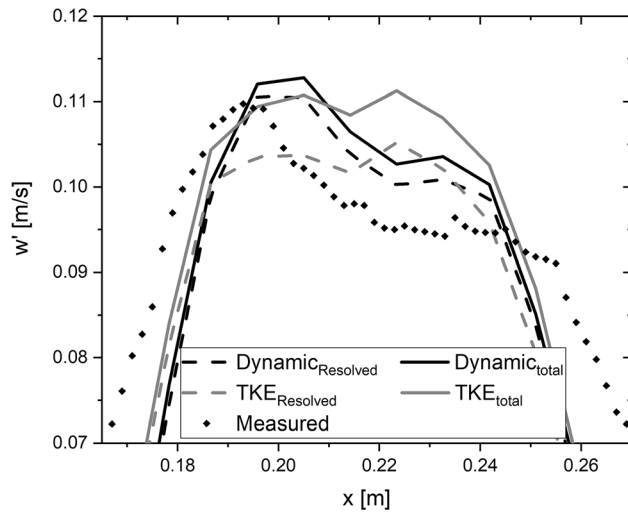Figure 3—Scores of the different subgrid turbulence models.

Figure 4—Resolved and total axial velocity fluctuation in the plume region by the dynamic Smagorinsky and the subgrid turbulent kinetic energy transport model.

profile of the axial velocity, which results in an overestimation of the axial velocity. In contrast to that, the finest grid showed almost no deviation compared to the medium mesh. In a subsequent study,[22] a value of 0.75 ($\Delta x = 3$ mm) was examined, but it also predicted very similar values. Fraga et al.[23] investigated three different grid resolutions for a bubble column with a bubble size of 2 mm. Ratios of $\Delta x/d_B = 3.125$ ($\Delta x = 6.25$ mm), 1.5 ($\Delta x = 3.125$ mm) and 1.25 ($\Delta x = 2.5$ mm) were compared. It was found that the coarse and medium grid yield almost similar results, while the finer grid estimates a lower bubble velocity and a wider spreading of the plume. The authors suspected that this is due to a finer resolution of the shear layer in the plume region.

In this study, three different grid resolutions are examined. For that, grids with a cell width to bubble diameter ratio of $\Delta x/d_B = 1.4$ ($\Delta x = 6$ mm), 1.2 ($\Delta x = 5$ mm) and 0.9 ($\Delta x = 4$ mm) are created. In addition, the effect of a simplification of the geometry is investigated by including the curvature in the water models bottom. Finally, the effect of a refinement of the

grid in the vicinity of walls is investigated. Thereby the cells adjacent to a wall have a thickness of 0.4 mm and grow along the walls normal by a ratio of 1.2 to the coarse grid resolution ($\Delta x = 6$ mm). Each grid is created with a centric O-grid to reduce the skewness of the cells.

The results are shown in Figure 5. It can be seen that the total score increases with the grid resolution. However, the reason for that is not monocausal. The coarse and the medium grid yield similar scores for the single-phase region, even though the contribution of the different subsystems changes. On the other hand, the multiphase subsystems, bubbles and plume both benefit from a grid refinement. In case of a fine grid, the bubble score does not further increase but the plume and the monitors score do. Interestingly, the toroid's score slightly decreases with a grid refinement, whereas the monitor's score increases.

For a more detailed analysis, the bubble rising velocity profiles (a) as well as the axial liquid velocity (b) for a height of $z = 0.36$ m are shown in Figure 6. It reveals that the spreading of the plume depends on the grid resolution, but mainly in case of the coarse grid. By approximating the bubble frequency over the x position, a standard deviation of 0.0249 m is found for the validation data, though this value might be slightly overestimated since the detection probability of the experimental method BubCNN decreases with increasing void fraction which is higher at the plume center.[24] The numerical models predict 0.0185 m ($\Delta x = 4$ mm), 0.0193 m ($\Delta x = 5$ mm) and 0.166 m ($\Delta x = 6$ mm), respectively. This shows that all models underpredict the plumes spreading but the effect depends on the grid resolution. A similar observation was made by Sungkorn et al.[22] and Fraga et al.[23] The latter assumed that this effect is caused by a better resolution of the shear layer which determines the lift force. This effect is further investigated throughout this study. The coarse grid overpredicts the axial liquid velocity, while the finest grid slightly underestimates it. The medium grid predicts the maximum axial velocity almost perfectly. However, it has to be considered that the different spreading of the bubbles also affects the plume velocity profiles. Because the spreading is underestimated with all grid resolutions, all velocity profiles are too narrow
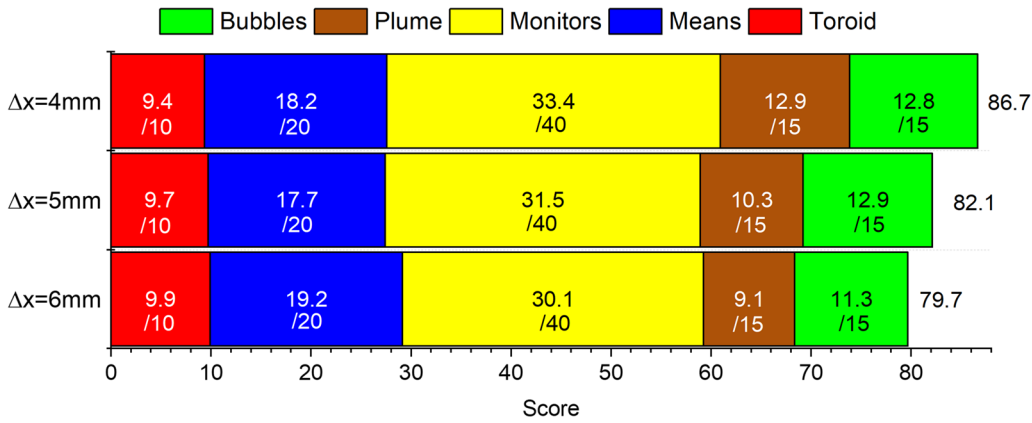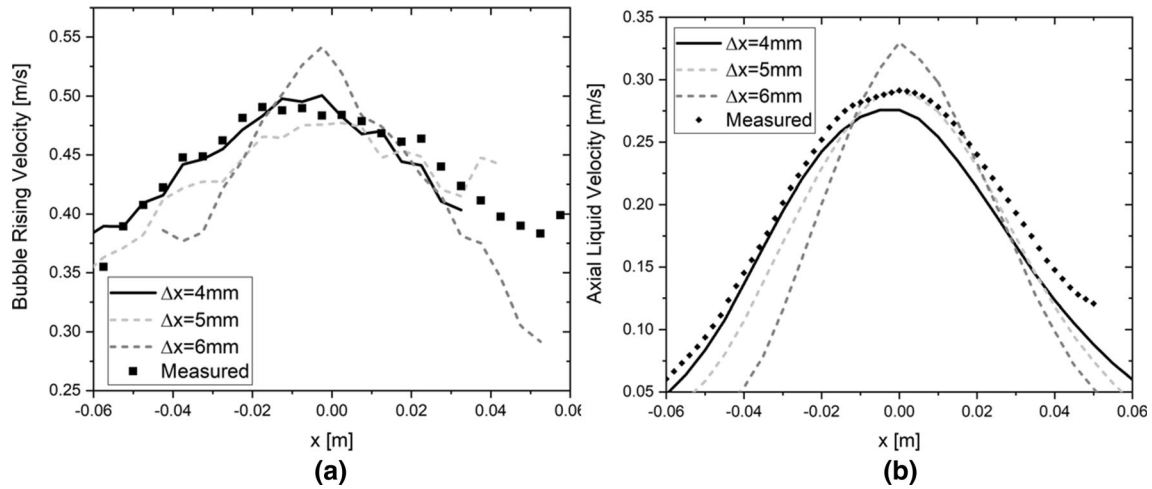
Figure 5—Scores of the different grid resolutions.

Figure 6—Bubble rising velocity (*a*) and axial liquid velocity (*b*) in dependence of the grid resolution ($z = 0.36$ m).

as well. Therefore, it can be assumed that the overall momentum transferred from the bubbles to the liquid is underpredicted.

The averaged axial velocity fluctuation in the plume at a height $z = 0.36$ m is shown in Figure 7 for the different grid resolutions. As expected, the proportion of modeled turbulent kinetic energy is lowest for the finest resolution. However, the resolved velocity fluctuation decreases as well. Therefore, it can be concluded that the total velocity fluctuation is grid dependent as well and is not sufficiently modeled with the subgrid turbulence model. This result contradicts the study of Sungkorn et al.[17] where the velocity fluctuation became grid independent in case the resolution was finer than $\Delta x/d_B = 1.5$ ($\Delta x = 6$ mm). The medium resolution represents the experimental data best, while a further refinement causes an underprediction of the velocity fluctuation.

The scores achieved with the modified grids are shown in Figure 8. Interestingly, a grid refinement in the vicinity of the walls significantly reduces the overall accuracy of the model. It is suspected that it is either because the CFL stability criterion is violated in this region or due to the high aspect ratio of the cells which
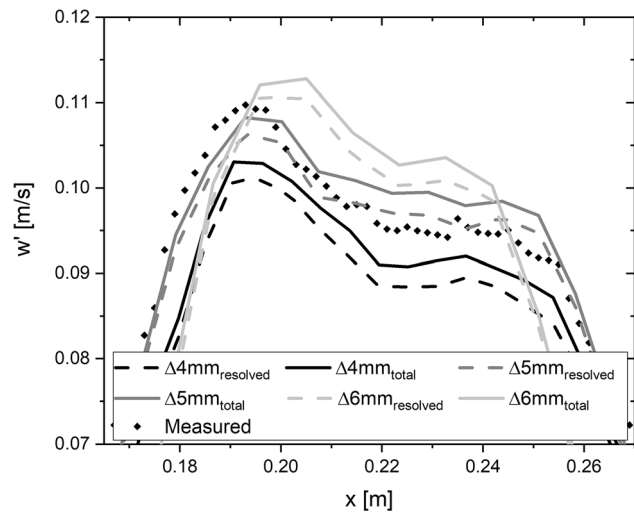

Figure 7—Resolved and total axial velocity fluctuation in the plume region by different grid resolutions ($z = 0.36$ m).

causes numerical instability. Here, the cells are only refined in the direction of the walls normal. However, additional studies with adaption layers and hanging

nodes should be conducted to figure out the cause of the accuracy reduction and whether different meshing strategies can be implemented to suppress this behavior.

Including the curvature in the bottom increases the accuracy, even though the overall accuracy in the main flow field decreases. This is mainly because the spreading of the plume near the injector is computed more accurately, resulting in a higher bubble score. This underlines the importance of the flow conditions at the vicinity of the injector on the bubble plume. On the other hand, the means and the toroid score fall, mainly because the means are slightly underpredicted. The results suggest that the geometry should not be simplified and curvatures or tapered walls should be modeled as such.

D. Averaged Shear Field Approach

The previous study revealed that the lateral spreading of the bubble column depends on the grid resolution. A similar observation was already made by Fraga et al.[23] The authors of this study attributed the effect to a changed resolution of the shear field. To further investigate that assumption, the averaged and instantaneous shear fields, represented by the $\partial u_z/\partial x$-component, are compared in Figure 9 for different grid resolutions. It shows that the averaged profiles are very similar, while the instantaneous profiles differ from one another. On the coarsest grid, the gradients of instantaneous $\partial u_z/\partial x$ along the x-direction are most pronounced because it is only computed at every cell center. For finer grids, $\partial u_z/\partial x$ becomes smoother. An explanation of the different spreading of the plume might be the stronger acceleration of bubbles on the coarser grid that is hindered by the virtual mass force.

Dhotre et al.[13] pointed out that the lift force requires a different formulation when using the LES model, since instantaneous velocities are computed. Ziegenhein et al.[25] showed experimentally that the instantaneous lift force differs from the averaged lift force. However, all available experimental results were established considering an averaged lift coefficient. To take this into account, an averaged shear field approach is proposed in this work. Instead of using the instantaneous components of the shear field, all components are averaged

over a longer period of time and these averaged values are used in Eq. [11]. By that, the formulation for the lift force becomes the same as for the RANS approach with the difference that the averaged shear components are independent variables that are only used for the modeling of the lift force, not for the conservation equations.

As shown in Figure 10, the averaged shear field approach results in almost grid independent bubble rising profiles (a) and axial liquid velocity profiles (b). For all grid resolutions, the bubble column becomes wider (σ_{4mm}: 0.0195 mm, σ_{5mm}: 0.0198 mm, σ_{6mm}: 0.0197 mm). On the macroscale the total score increases, but this effect is more pronounced for the coarsest grid. For the coarse grid the score rises from 79.7 to 82.4, for the medium grid from 82.1 to 82.9 and for the fine grid from 86.7 to 87.8. On the other, the methods require further investigation. As it can be seen by a comparison of Figure 6 and Figure 10, the bubble rising velocity increases, especially in the plume center. This is because not only the radial components of the lift force increase but also the axial ones, resulting an increase bubble acceleration.
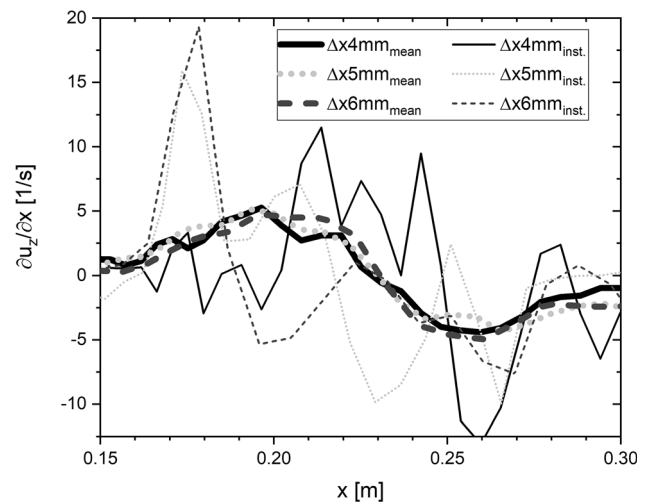

Figure 9—Averaged and instantaneous shear field represented by $\partial u_z/\partial x$ for different grid resolutions ($z = 0.36$ m).
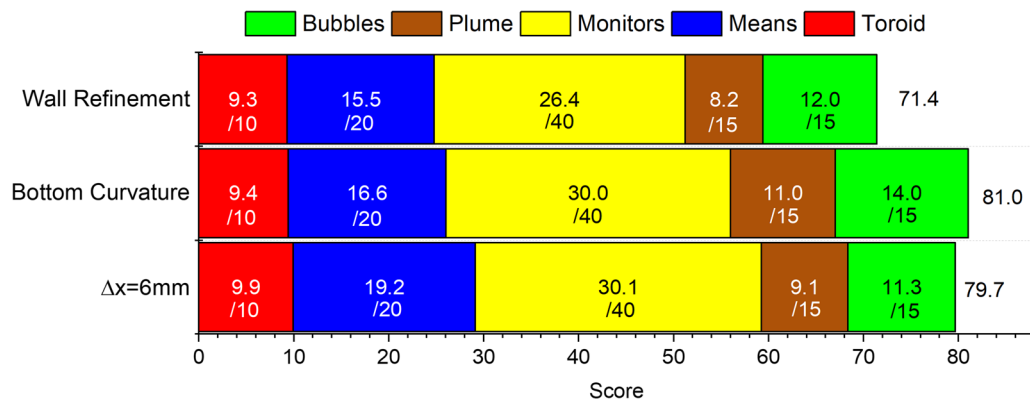

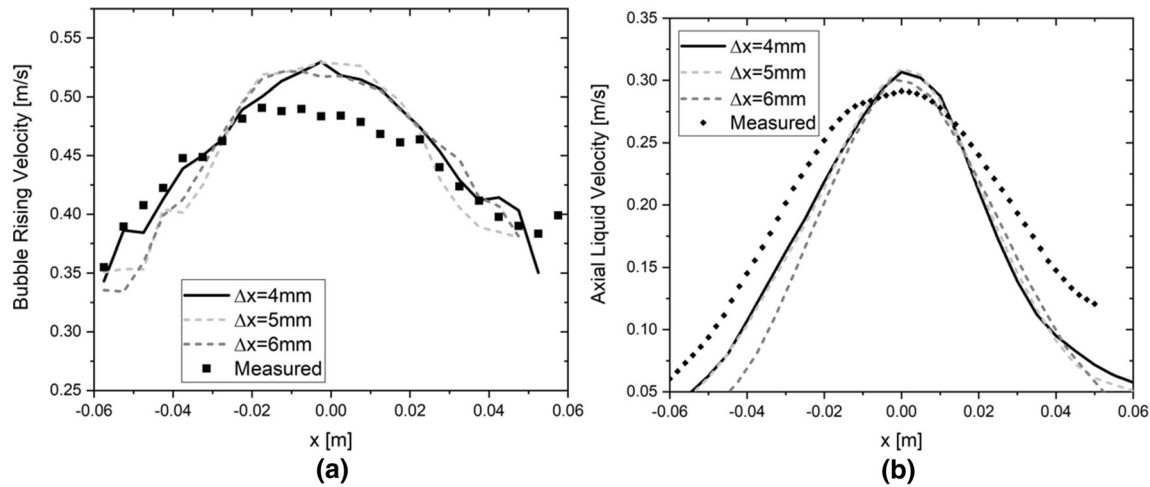Figure 8—Scores of the different meshing strategies.

Figure 10—Bubble rising velocity (*a*) and axial liquid velocity (*b*) in dependence of the grid resolution with the averaged shear field approach (*z* = 0.36 m).

Nonetheless, to reduce the computational effort, all subsequent studies are carried out on the coarse grid employing the averaged shear field approach.

E. Bubble-Induced Turbulence

Bubbles contribute to the turbulence in the plume region and can even alter the turbulent energy cascade. In numerical modeling of the ladle in conjunction with the standard k–ε model, different studies confirmed for the quasi-single-phase model,[26,27] the E–L[28–30] and the E–E[31] model that the inclusion of bubble-induced turbulence (BIT) increase the accuracy of the numerical model. LES turbulence model is better suit to account for bubble effects on the turbulence. Nonetheless, most phenomena are microscale effects that cannot be modeled directly on the grid. Thus, it has to be considered in the subgrid model. Therefore, the concept of BIT as an additional source term in the transport equation of the subgrid turbulent kinetic energy (Eq. [A3]) is investigated. For E–E LES, Niceno *et al.*[16] implemented different approaches to model BIT and concluded that the model by Pfleger and Becker[32] improves the accuracy of the numerical model, in particular in regards to the turbulent kinetic energy. To the best of the authors knowledge, there is no study hitherto investigating the influence of the BIT on the E–L LES approach. In this work, a recent formulation by Ma *et al.*[33] is used:

$$S_k^{BIT} = min\big(0.18 Re_B^{0.23}, 1\big) \bullet \overrightarrow{F}_F^{Drag}(\vec{u}_B - \vec{u}_F) \qquad [19]$$

The scores of the model including the BIT and without BIT are given in Figure 11. Including BIT lowers the overall accuracy though the effect on the main flow field is very low. In the plume region, the higher turbulent viscosity damps the flow, providing a closer agreement of the axial liquid velocity in the vicinity of the injector. That results in a higher plume score. On the other hand, the damping is too strong in the other regions of the plume which causes an underprediction of the bubble rising velocity.

For a more detailed analysis, the averaged fluctuation of the axial fluid velocity is shown in Figure 12. Similar to the study of Niceno *et al.*,[16] the BIT is found to produce more distinct double peaks. In addition, it captures the asymmetry of the peaks which cannot be found in case the subgrid turbulent kinetic energy transport model is employed without an additional BIT source term. On the other hand, the BIT source term increases the overestimate of the total velocity fluctuation because the subgrid part increases. Thus, it can be concluded that the inclusion of a BIT source term gives a better representation of the axial velocity fluctuation profile, but for the given case it decreases the accuracy by increasing the overestimate. However, as shown in Figure 7, the axial liquid velocity depends on the grid resolution. It can be speculated that for the fine grid the inclusion of BIT would increase the match between numerical model and the experiment. Because of that, further studies regarding the implementation of the source term as well as the grid resolution are necessary for a final assessment of that effect.

F. Initial Bubble Size

The effect of the initial bubble size is investigated next. Even if this value is known for the water model from the experimental database, this does not apply to the real plant. As shown in Table II, the bubble size in the ladle can vary depending on the correlation used, leading to potential challenges in the upscaling of experimental and numerical results.

In addition, the choice of the injector type has a significant influence on the bubble size distribution.[37,38] Experimentally it was found that this in turn can have an influence on the flow in the single-phase region.[39] In this work, the effect of smaller (d_B = 2.9 mm) and
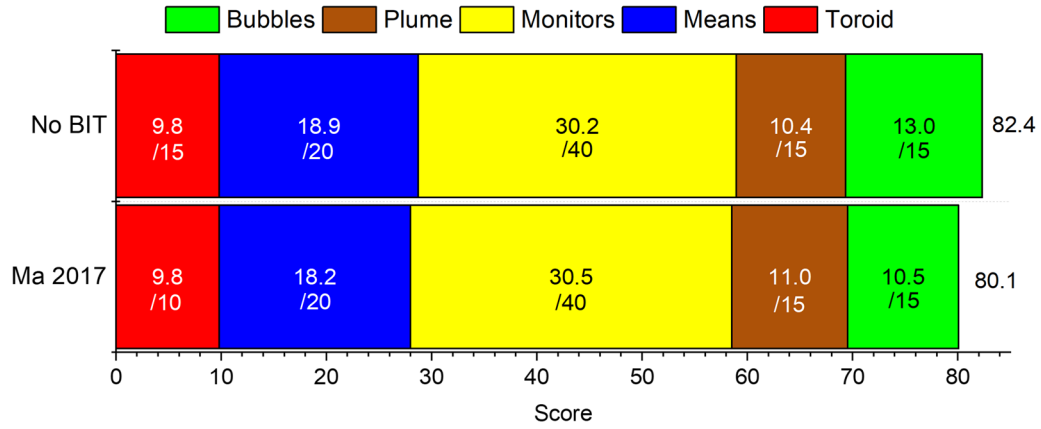
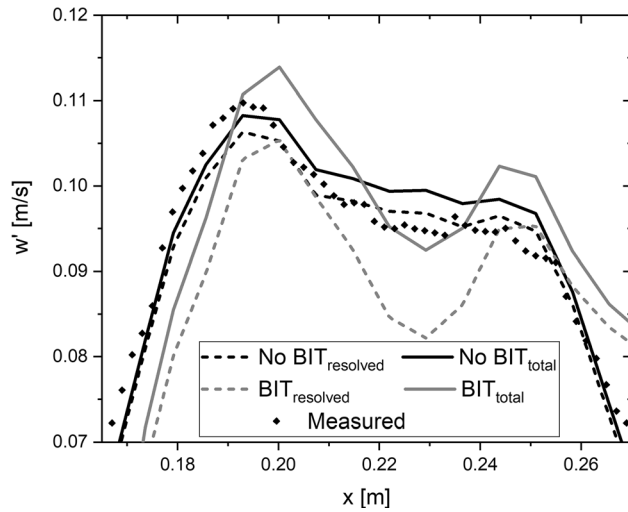Figure 11—Scores without and with bubble-induced turbulence.

Figure 12—Resolved and total axial velocity fluctuation in the plume region with and without bubble-induced turbulence ($z = 0.36$ m).

Table II.   Bubble Size Correlations for the Steel Casting Ladle

Source	Equation	$d_{B,ladle}$ (mm)
[34]	$d_{B,L} = d_{B,M} \sqrt{\frac{\sigma_B (\rho_F - \rho_B)_M}{\sigma_M (\rho_F - \rho_B)_L}}$	8.5
[35]	$d_B = 1.46 \left[\frac{\dot{V}_{g,z}}{z + H_0} \right]^{0.1}$	18.2
[36]	$d_B = \left[\left(\frac{6 \sigma d_n}{\rho_F g} \right)^2 + 0.0242 \left(Q_g^2 d_n \right)^{0.867} \right]^{1/6}$	31.2

Subscripts M and L represent model and ladle, d_n is the pore size of the porous plug, H_0 is the distance between the nozzle and the mathematical origin of the plume, Q_g is the flowrate in m^3/s and $V_{g,z}$ the flowrate in cm^3/s.

larger ($d_B = 2.9$ mm) bubble sizes, as well as the modeling of the bubble size distribution according to the database is investigated. The results are shown in Figure 13.

It is found that the bubble size has a significant influence on the accuracy of the numerical model. An increase (score: 68.0) of the mean bubble size compared to the experimentally measured bubble size distribution results in a significant decrease of the accuracy. The effect is mainly because the multiphase scores diminish, but a small reduction of the single-phase accuracy can be observed as well. This can be explained by a change of the bubble column mode from homogeneous to heterogeneous, indicated by a significant reduction of the bubble spreading ($\sigma_{dB = 5.8 \text{ mm}} = 0.0083$ m). The influence of the bubble column mode on the main flow field was also found experimentally.[38] Lucas et al.[40] pointed out that this effect is correlated with the sign change of the lift coefficient, which takes places at a bubble size of 5.8 mm for the lift correlation of Tomiyama et al. For smaller bubble sizes (score: 79.9) the accuracy of the model remains almost constant, because the bubble column mode is not affected. The implementation of a bubble size distribution slightly increases the total score, mainly because the spreading of bubbles increases.

G. Lift Force

Subsequently, a systematic analysis of the interfacial closure models is conducted. It should be noted, that these models are not independent of one another and are also afflicted by the turbulence model, subgrid model or the grid resolution. However, to limit the number of computations, they will be investigated independently. All forces are studied on a coarse grid, with a bubble size distribution and the lift force is computed based on the averaged shear field approach.

The lift force is investigated first since it determines the lateral spreading of the plume which is important for the subsequent analysis of the drag closure. The effect of four different correlations for the lift coefficient is investigated, $C_L = 0.5$, which is the analytical value for spherical bubbles in inviscid flows,[41] $C_L = 0$ and the correlations by Tomiyama et al.[10] (Eq. (12)) and
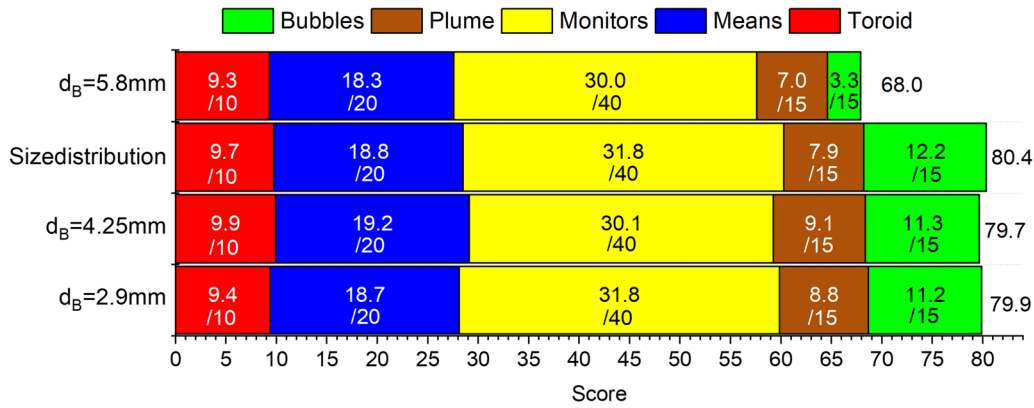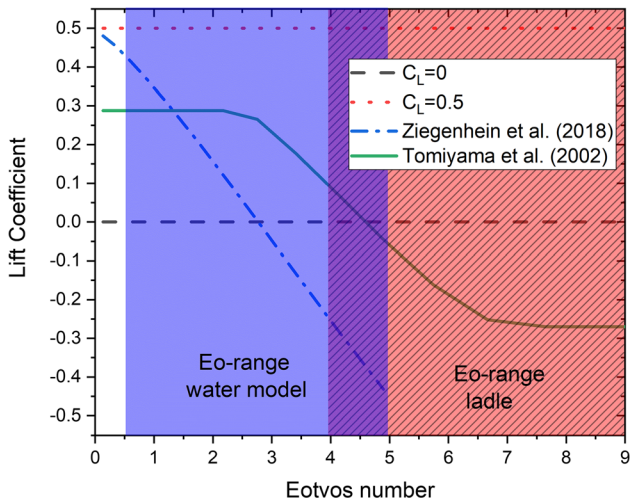
Figure 13—Scores of the different initial bubble sizes.

Figure 14—Different lift coefficient correlations in dependency of the Eotvos number.

Ziegenhein et al.[25] (Eq. (20)). The lift coefficient for these correlations is plotted against the Eotvos number in Figure 14.

As shown in Figure 14, in the empiric correlations by Tomiyama et al.[10] and Ziegenhein et al.[25] C_L exhibits a sign change. This is in line with observations, that large bubbles gather in the middle of the plume, while smaller bubbles are found more frequently at its outlines.[9] According to the current state of knowledge, the physical cause of this sign change is due to the fact that the lift force arises from two different effects. One effect is induced by a shear flow, the other by a complex interaction between the bubble wake and the shear flow which leads to a slanted wake.[42] The latter effect increases with increasing bubble size and bubble deformation as those factors affect the wake structure. Although these effects are quite different, both can be mathematically described similarly[10] and can therefore be incorporated in the lift coefficient C_L in Eq. [11].

Hitherto, CFD models for the ladle mostly neglect the lift force ($C_L = 0$). In case the lift force was considered it was either assumed to be constant for all bubbles ($C_L = 0.5$) or the Tomiyama correlation was employed,

which was derived from experiments in highly viscous liquids. More recent experimental studies for wider ranges of Morton numbers revealed that the Tomiyama model is only applicable in the range at which it was correlated.[43] Because of that, Ziegenhein et al.,[25] investigating the lift coefficient in an air-water system and correlated:

$$c_L = 0.5 - 0.1 Eo_d + 0.002 Eo_d^2, 1.2 < Eo_d < 10.5 \quad [20]$$

For smaller modified Eotvos numbers, Dijkhuizen et al.[44] showed that the correlation by Legendre and Magnaudet[45] for spherical bubbles gives reasonable results:

$$c_L = \sqrt{\left(\frac{6J(Re, Sr)}{\pi^2 \sqrt{Re * Sr}}\right)^2 + \left(\frac{1}{2}\frac{Re + 16}{Re + 29}\right)^2} \quad [21]$$

where the dimensionless shear rate Sr and $J(Re, Sr)$ are given by

$$J(Re, Sr) = \frac{2.255}{\left(1 + 0.2\frac{Re}{Sr}\right)^{3/2}} \quad [22]$$

$$Sr = \frac{\omega d}{|u_p - u_f|} \quad [23]$$

Since it was found that the lift coefficient scales with the modified Eotvos number rather than the Eotvos number, there is a need for a correlation of the bubble deformation. Tomiyama et al.[10] proposed to employ Eq. (15) by Wellek et al.[12] which was originally derived for liquid droplets. Ziegenhein et al.[25] reported that this correlation underestimated the measured major axes in an air-water system and proposed to use the same correlation but with other fitting parameters as shown in Figure 15. In Figure 14, the lift coefficient is computed in dependency of the major axis correlation proposed in their respective study.

The results of the simulations with different lift coefficients are shown in Figure 16. It can be seen that the overall scoring for the Tomiyama model or a constant lift coefficient of 0.5 exceed those of the
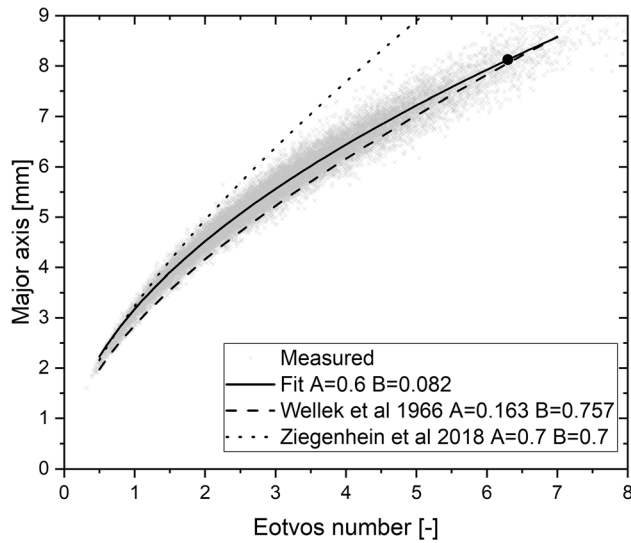
Figure 15—Bubble deformation in dependency of the Eotvos number.

Ziegenhein correlation or without the lift force. This is mainly, but not exclusively, because of the different scoring in the plume region. For a further analysis, the bubble rising velocity (a) and the axial liquid velocity (b) are given in Figure 17. While a constant lift coefficient ($\sigma = 0.02$ m) and the Tomiyama correlation ($\sigma = 0.0197$ m) underpredicts the plume's spreading slightly, the Ziegenhein correlation ($\sigma = 0.014$ m) and an exclusion of the lift force ($\sigma = 0.006$ m) predicts very narrow plumes. In addition, the accuracy of the single-phase region becomes smaller, most probably because of the previously discussed mode transition from homogenous to heterogenous bubble column. Interestingly, the correlation by Ziegenhein et al. leads to a decrease in the validation score compared to the Tomiyama model although this correlation was derived in an air-water system. This result can be explained by the fact that in the work of Ziegenhein et al.[25] deionized water was used, while the validation experiments were carried out with tap water and tracer particles. As it can be seen in Figure 15, these contaminants lead to a
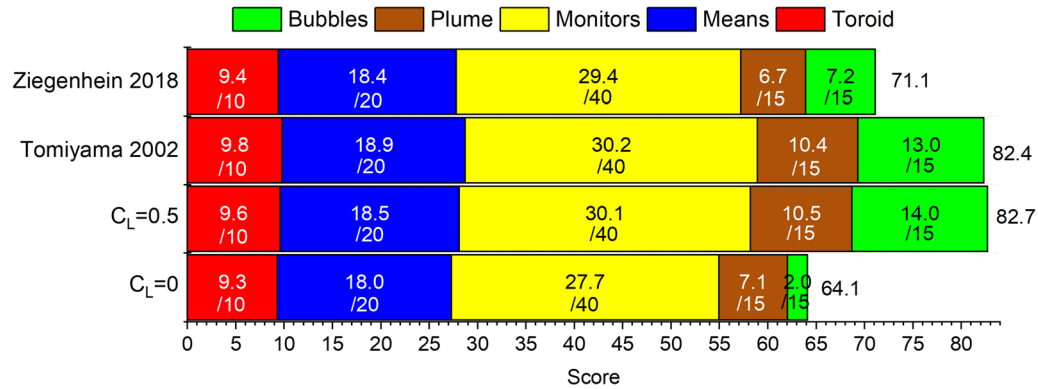

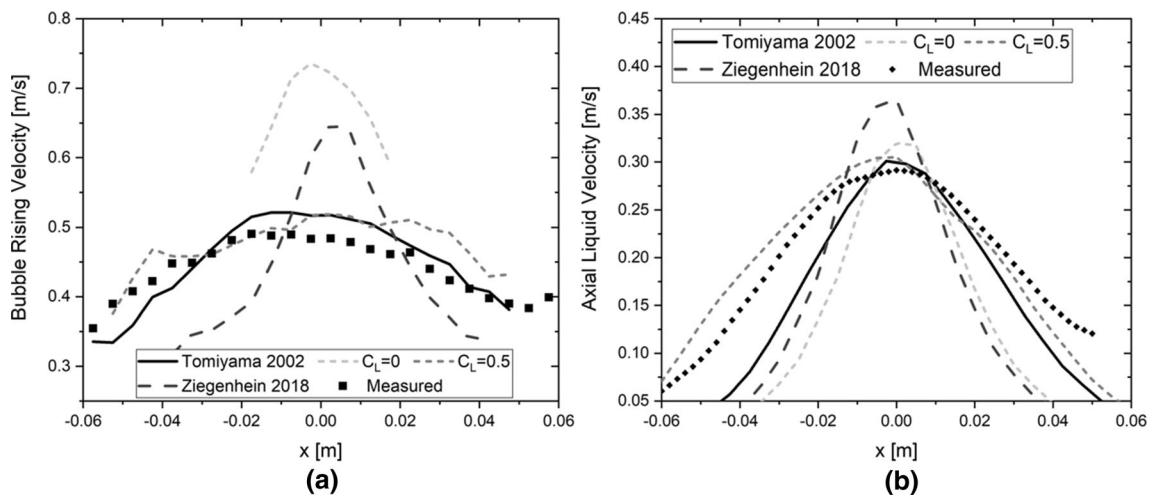Figure 16—Scores obtained with different lift coefficient correlations.

Figure 17—Bubble rising velocity (*a*) and axial liquid velocity (*b*) obtained with different lift correlations ($z = 0.36$ m).

significant decrease of the bubble deformation and thus probably also to a decrease of the lift coefficient. This result might suggest that the influence of contaminants is more significant than that of the Morton number, because it affects both, the bubble deformation and the dependency of the lift coefficient from the modified Eotvos number. Unfortunately, this effect is far from a comprehensive understanding and no mathematical correlations for its effect are available.

H. Drag Force

The drag force determines the bubble rising velocity and is the main contribution to the momentum transfer from bubbles to liquid. It comprises two phenomena, a viscous friction force and a force caused by a pressure gradient along the bubble surface in the direction of movement. The local pressure gradient is the result of the bubble wake and is therefore more pronounced in case of high bubble Reynolds numbers.

Because the bubble deformation and the wake structure are correlated, Bozzano and Dente[46] argued that the drag depends on the bubble deformation and proposed:

$$C_D = f\left(\frac{a}{R_{eq}}\right)^2 \qquad [24]$$

where f is a friction factor, R_{eq} is the equilibrium bubble radius and a is the bubble major semi-axis. Equations for these parameters can be found in the original paper.[46]

By direct numerical simulation Dijkhuizen et al.[47] proposed for ultra-purified liquids:

$$C_D = \sqrt{C_D(Re)^2 + C_D(Eo)^2} \qquad [25]$$

where $C_D(Re)$ is the analytical correlations for spherical bubbles by Mei and Klausner[48]:

$$C_D(Re) = \frac{16}{Re}\left(1 + \frac{2}{1 + \frac{16}{Re} + \frac{3.315}{\sqrt{Re}}}\right) \qquad [26]$$

and $C_D(Eo)$ takes account for the deformation of larger bubbles:

$$C_D(Eo) = \frac{4Eo}{Eo + 9.5} \qquad [27]$$

The drag coefficients of the three investigated drag correlations are plotted against the Eotvos number in Figure 18. Because the correlation of Bozzano and Dente contains a Morton-dependent term, it is plotted for water and steel (Figure 19).

The aforementioned studies were derived from the rise of single bubbles. However, it was found that the presence of other bubbles affects the drag force. To account for that, Roghair et al.[49] proposed to include the swarm effects by

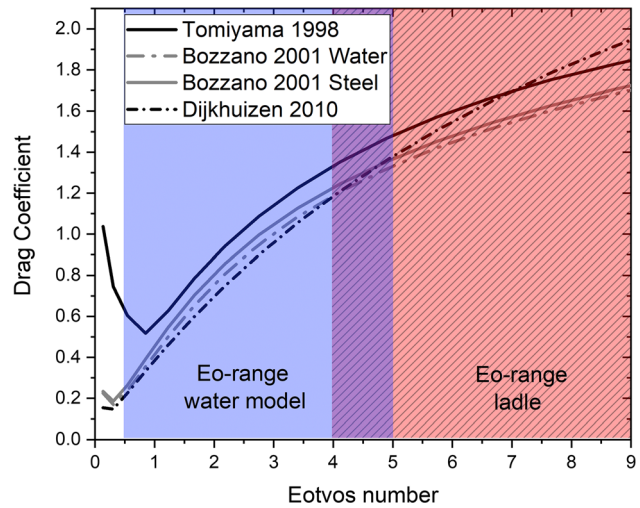$$C_{D,swarm} = C_D(1 - \alpha)\left(1 + \frac{18\alpha}{Eo}\right), \qquad [28]$$

Figure 18—Different drag coefficient correlations in dependency of the Eotvos number.

where α is the void fraction. Since that value is not directly accessible with the E–L approach, it is computed for each bubble individually by dividing the volume covered with other bubbles within an influencing sphere by the volume of that influencing sphere. The influencing sphere is chosen to have four times the diameter of the bubble. However, it should be noted that the result might be influenced by its implementation and the diameter of the influencing sphere. For C_D, the correlation by Tomiyama et al. (Eq. (10)) is used, though in the original paper the correlation of Dijkhuizen et al. (Eq. (25)) was proposed.

The scores of the different correlations are summarized in Figure 20. The scores in the single-phase region are very similar and no clear trend can be seen. The main difference arises from the bubble score where the correlation of Tomiyama yields the highest score and from the plume score for which the inclusion of swarm effects performs best. However, the total scores for all correlations are quite similar. Therefore, it can be concluded that the accuracy is less sensitive to the drag force than to the lift force.

A more detailed analysis is made by comparing the bubble rising velocity (a) and the axial fluid velocity (b), shown in Figure 20. It can be seen that all models overestimate the bubble rising velocity, while the fluid velocity is underestimated. This indicates that the drag coefficient is too low in all models, and thus bubbles and fluid are too weakly coupled. As expected, the Tomiyama model shows the best agreement as it predicts the highest drag coefficient in the investigated range of the three models tested. This observation is in line with numerical results of Frank et al.[11] and experimental measurements by Bröder and Sommerfeld.[50] The correlation of Bozzano and Dente[46] underestimates the drag force because it overestimates the bubble deformation which is lowered by the presence of contaminants and tracer particles in the experiments. Similarly, the correlation of Dijkhuizen et al.[47] was
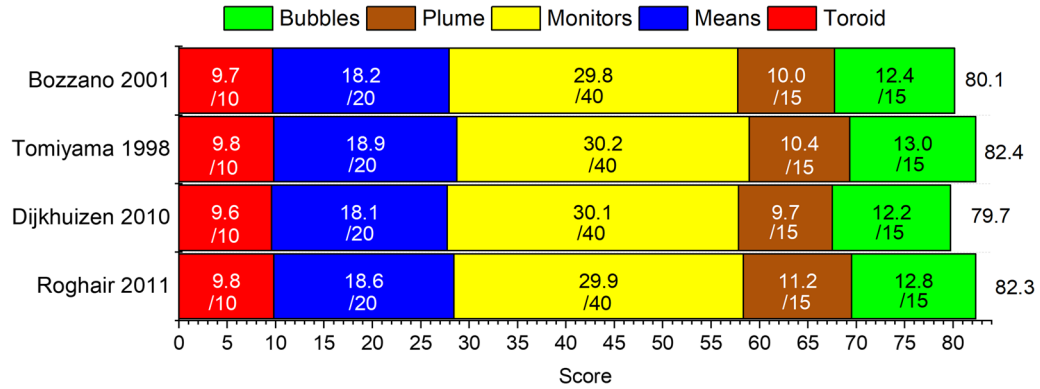
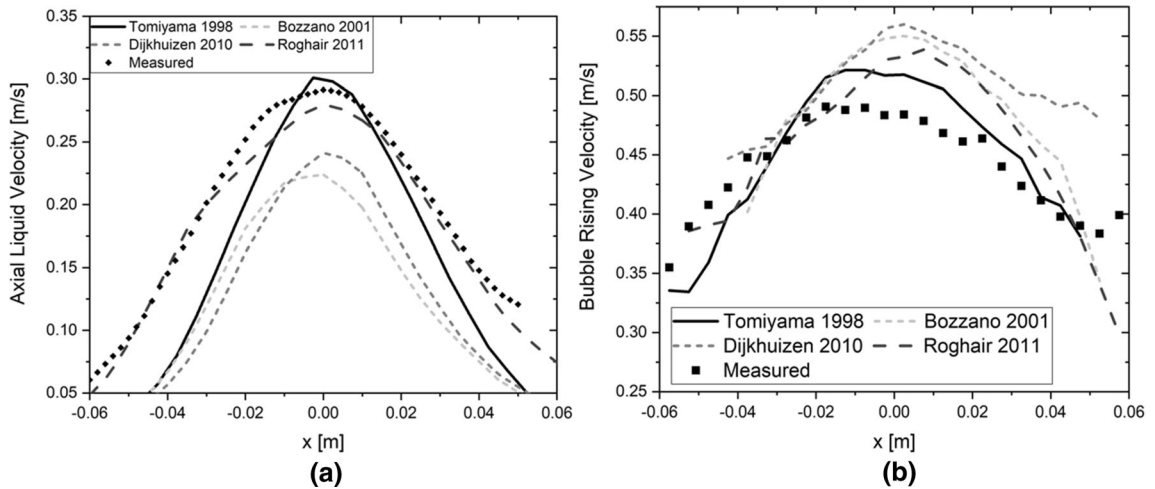Figure 19—Scores obtained with different drag coefficient correlations.

Figure 20—Bubble rising velocity (*a*) and axial liquid velocity (*b*) obtained with different drag correlations ($z = 0.36$ m).

derived for ultra-purified liquids, thus, it does not consider the effects of contaminations. The inclusion of swarm effects provides a similar bubble rising velocity profile to the correlation of Tomiyama. Thus, it can be concluded that the swarm effect is small, though it should be noted that this might be due to its implementation.

Interestingly, it was reported for the validation experiments[5] that the bubble rising velocity without solid tracer particles is about 10 pct higher compared to a liquid without seeding. The term 'fully contaminated' in the work of Tomiyama *et al.*[8] refers to the influence of contaminants, not to the effect of solid particles. Therefore, it can be assumed that solid particles cause an additional increase of the drag coefficient, which is not considered in the models. Similar to the lift force, this leads to problems in upscaling, since it is unknown how alloying elements and non-metallic inclusions influence the drag coefficient. Another explanation of the overestimated bubble rising velocity might be the additional force arising from the axial component of the lift force, which is higher in case the averaged shear field approach is employed.

IV. UPSCALING CHALLENGES

Since the optimization potential through numerical simulation is limited by the accuracy of the models, a comprehensive analysis of different submodels was carried out in this work. Through various measures the validation score could be increased from 38.7 to 85.1 on a coarse grid and 87.8 on a fine grid. However, apart from these improvements, the study also shows problems in the upscaling of the numerical model from the water model to the real ladle, which were often overlooked hitherto.

Further investigations of the influence of the numerical grid on the solution are required. As described in this study, the opposing grid requirements of the E–L model and the LES model as well as the numerical error have to be fulfilled simultaneously. For that, more elaborate mapping techniques for the E–L model need to be found. Furthermore, the efficiency of the calculation has to be considered. To model the real process, the computational effort increases by a factor of 125 for the same grid resolution. Probably a longer calculation time is necessary because the characteristic dimension of the main flow increases. By that, a single calculation would
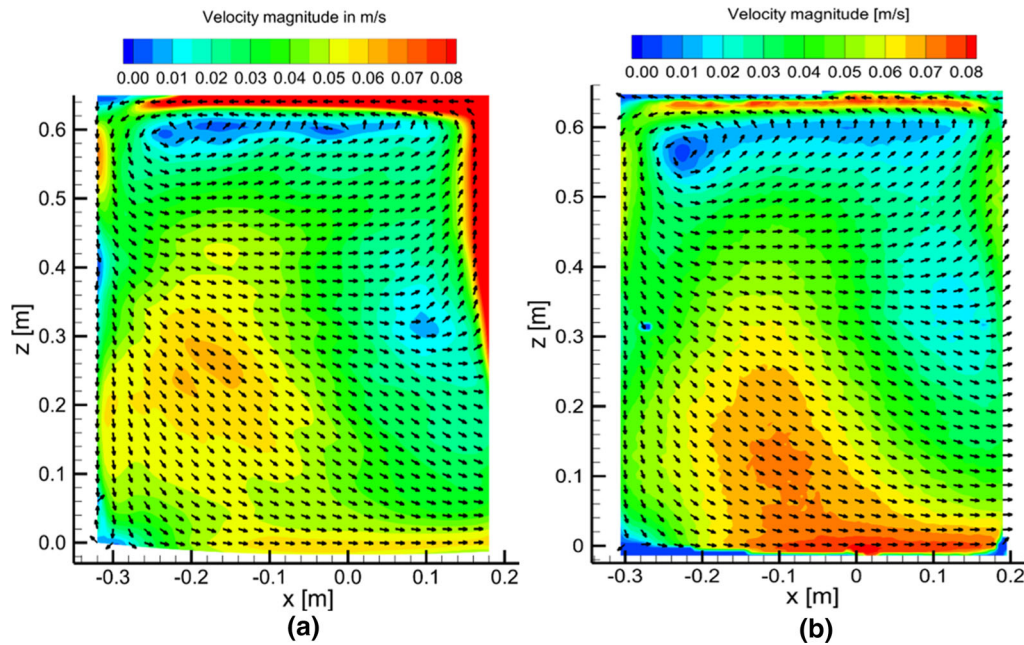
Figure 21—Numerical (*a*) and measured (*b*) velocity profile on the symmetry plane.
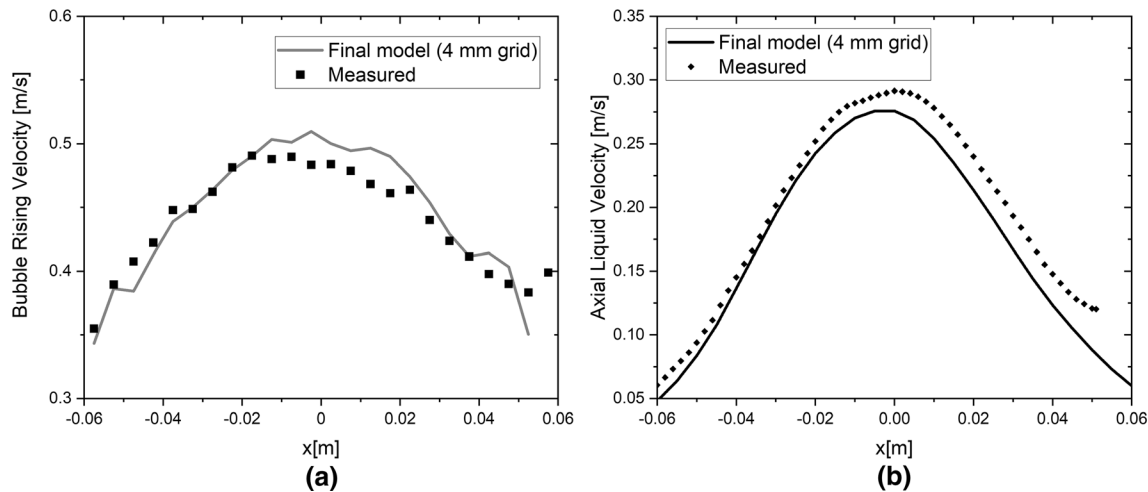

Figure 22—Bubble rising velocity (*a*) and axial liquid velocity (*b*) obtained with the model of highest validation score ($z = 0.36$ m).

take months. This clearly shows that a more efficient meshing strategy must be found. The averaged shear field approach presented here reduces the grid dependency in the bubble region, but further studies are necessary, especially with regard to the larger bubble size in the real process. Other studies have to find the ideal tradeoff between accuracy and computational effort. Presumably, hybrid meshes will be needed that allow different resolution in the different zones of the ladle and still provide an aspect ratio of about 1 and the lowest possible distortion. It can be assumed that the resolution in the isotropic single-phase region can be reduced to a certain limit, but a dimensionless criterion for this limit has to be found. For the plume region, the phase boundary and probability also the near-wall region, a grid refinement has to be made but ideal values have to be found here as well.

Another uncertainty factor arises from the influence of alloying elements and non-metallic inclusion on the dynamics of the bubble column. As known from the literature and shown in this study, impurities and solid particles have an influence on bubble deformation, lift and drag force. So far, studies on these effects in liquid metals are completely lacking. Especially when these effects lead to a transformation from a homogeneous to a heterogeneous bubble regime, this can have an influence on the flow. For the same reason it is also important to know the exact bubble size distribution in the real process. Furthermore, the interfacial closure correlations have usually been derived in aqueous systems with higher Morton numbers than liquid steel. Especially the surface tension is significantly lower. Therefore, an extrapolation of these models to the ladle can be highly inaccurate. For instance, Wellek *et al.*[12]

pointed out that the bubble deformation is not only a function of the Eotvos number but also of the Morton number. Ziegenhein *et al.*[25] showed that the Eotvos number at which the sign change occurs is a function of the Morton number as well.

V. CONCLUSION

The results of the different subsystem studies are summarized to a best-practice guideline for the modeling of the isothermal flow in the ladle. Best results are obtained in case the geometry is not simplified, so it is advisable to consider bottom curvatures or tapered walls. The turbulence model should be the LES model to take account for the anisotropy of the turbulence in the plume region. The best representation of the bubbles and the axial liquid velocity in the plume region is maintained by the implementation of a bubble size distribution and by employing the Tomiyama drag model (Eq. [10]) for fully contaminated systems and the Tomiyama lift model (Eq. [12]) with the bubble deformation model by Wellek *et al.* (Eq. (15)). However, further research is necessary for a better understanding of the effect of contaminants and swarm effects on the interfacial closure and of the grid dependency of its implementation. Since LES computes the instantaneous flow rather than the averaged, the following procedure should be applied to obtain a correct averaged flow field. The solutions should be computed for 30 seconds physical times before starting the averaging procedure for the shear field in the plume region. After further 30°s, the sampling of the flow variables can be started. Sampling should be maintained for 120 seconds for a small residual uncertainty.

With these measures, a final validation score of 85.1 for a coarse grid respectively 87.8 on a fine grid is achieved. Since the validation score is not yet a fully established validation tool, a standard comparison of the final model with the highest validation score and the validation data is provided in Figures 21 and 22. A comparison of the single-phase flow field on the symmetry plane calculated with the numerical model (Figure 21(a)) and experimentally measured (Figure 21(b)) shows almost equal flow patterns and only minor deviations of the flow magnitude. By a comparison of the bubble rinsing velocity (Figure 22(a)) and the axial liquid velocity (Figure 22(b)) it can be seen that the bubble rising velocity is slightly overpredicted, while the liquid velocity is underpredicted. However, the deviations are almost within the measurement uncertainty of the validation experiments.[5]

APPENDIX

Subgrid Turbulent Models

Following the mixing-length concept, Smagorinsky[14] proposed:

$$\mu_{\text{t}} = \rho_{\text{F}} L_{\text{s}}^2 \sqrt{S^2} \qquad [\text{A1}]$$

where L_{s} is the mixing-length for subgrid scales, estimated as local variable with the Germano approach refined by Lilly.[51] S is the characteristic strain tensor of the filtered velocity (Table A1).

Deardorff [15] proposed an analogy to the k–ε model:

$$\mu_{\text{t}} = C_{\text{k}} \sqrt{k_{\text{sgs}}} \Delta_{\text{f}} \qquad [\text{A2}]$$

where Δ_{f} is the LES filter size and k_{sgs} is the subgrid turbulent kinetic energy obtained by the transport equation:

$$\frac{\partial k_{\text{sgs}}}{\partial t} + \frac{\partial \overline{u}_j k_{\text{sgs}}}{\partial x_j} = -\tau_{ij} \frac{\partial \overline{u}_i}{\partial x_j} - C_\varepsilon \frac{k_{\text{sgs}}^{\frac{3}{2}}}{\Delta_{\text{f}}} + \frac{\partial}{\partial x_j}\left(\frac{\mu_{\text{t}}}{\sigma_k}\frac{\partial}{\partial x_j}\right) \ [\text{A3}]$$

C_k in Eq. (A2) and C_ε in Eq. (A3) are model constants dynamically adjusted by the method proposed by Kim and Menon.[52]

Computation of Velocity Fluctuation Components

The total velocity fluctuation is given by

$$w'_{\text{total}} = \sqrt{\left(w'_{\text{resolved}}\right)^2 + \left(w'_{\text{sgs}}\right)^2} \qquad [\text{A4}]$$

Based on the assumption of an isotropic subgrid turbulence, the subgrid axial velocity fluctuation w'_{sgs} can be obtained by

Table A1. List of Symbols and Abbreviations

Symbol	Description
a	bubble major semi-axis in Bozzano drag model, m
C_D	drag coefficient
C_k	model constant
C_L	lift coefficient
C_{VM}	virtual mass coefficient
C_ε	model constant
$d_{B,0}$	initial bubble diameter, m
$d_B(z)$	bubble diameter at height (z), m
d_h	length of bubble major axis, m
d_n	pore size of porous plug, m
Eo	Eotvos number
Eo_d	modified Eotvos number
$F_{B,i}$	mass-based force i on bubble, N
$\vec{F}_{ex}$	exchanged momentum from bubble to fluid, N
F_n	volume fraction of phase n
f	friction factor in Bozzano drag model
g	gravity, 9.81 m/s^2
H_0	distance between nozzle and the mathematical origin of the nozzle, m
H_{Fill}	filling height, m
k_{sgs}	subgrid turbulent kinetic energy, m^2/s^2
L_s	mixing-length for subgrid scales, m
m_B	bubble mass, kg
p_0	atmospheric pressure, N/m^2
Q_g	gas flow rate in m^3/s
R_{eq}	equilibrium bubble radius in Bozzano drag model, m
Re_B	bubble Reynolds number
S_k^{BIT}	turbulent kinetic energy source by bubble-induced turbulence
Sr	dimensionless shear rate
$\vec{u}_B$	bubble velocity, m/s
$\vec{u}_F$	fluid velocity, m/s
$\vec{u}_i$	fluid velocity component i, m/s
$\dot{V}_{g,z}$	gas flow rate, cm^3/s
w'_{total}	total velocity fluctuation, m/s
$w'_{resolved}$	resolved velocity fluctuation, m/s
w'_{sgs}	subgrid velocity fluctuation, m/s
$\vec{x}_B$	coordinate of bubble
$\vec{x}_n$	coordinate of computation node
Δx	cell width, m
α	void fraction
μ_F	fluid viscosity, Ns/m^2
μ_t	turbulent viscosity, Ns/m^2
ρ_B	bubble density, kg/m^3
ρ_F	fluid density, kg/m^3
Σ	surface tension, N/m
σ_{4mm}	bubble column width for a grid resolution of 4 mm, mm
σ_{5mm}	bubble column width for a grid resolution of 5 mm, mm
σ_{6mm}	bubble column width for a grid resolution of 6 mm, mm

Abbreviation	Description
BIT	bubble-induced turbulence
CFD	computational fluid dynamics
CFL	Courant–Friedrichs–Lewy number
E–E	Euler–Euler multiphase approach
E–L	Euler–Lagrange multiphase approach
LES	large eddy simulation
RANS	Reynolds-average Navier–Stokes
VOF	volume of fluid model

$$w'_{\text{sgs}} = \sqrt{\frac{2}{3} k_{\text{sgs}}} \qquad [\text{A5}]$$

where k_{sgs} is the subgrid turbulent kinetic energy which is directly accessible in the subgrid turbulent kinetic energy transport model. In the dynamic Smagorinsky model it can be computed by

$$k_{\text{sgs}} = \left(\frac{\mu_{\text{t}}}{\rho_{\text{F}} L_{\text{S}}} \right)^2 \qquad [\text{A6}]$$

REFERENCES

1. D. Mazumdar and R.I.L. Guthrie: *ISIJ Int.*, 1995, vol. 35, pp. 1–20.
2. Y. Liu, M. Ersson, H. Liu, P.G. Jönsson, and Y. Gan: *Metall. Mater. Trans. B*, 2019, vol. 50B, pp. 555–77.
3. T. Haas, M. Eickhoff, and H. Pfeifer, in *8th International Conference on Modeling and Simulation of Metallurgical Processes in Steelmaking (STEELSIM 2019)*, Toronto, 2019.
4. T. Haas, A.L. Suarez, M. Eickhoff, and H. Pfeifer: Towards a strong-sense validation benchmark database for numerical ladle flow models. *Metall. Mater. Trans. B*, 2020. https://doi.org/10.18154/RWTH-2020-03939.
5. T. Haas, A.L. Suarez, M. Eickhoff, and H. Pfeifer: *Metall. Mater. Trans. B*, 2021, vol. 52, pp. 199–222.
6. K. Krishnapisharody and G.A. Irons: *Metall. Mater. Trans. B*, 2013, vol. 44, pp. 1486–98.
7. C.W. Hirt and B.D. Nichols: *J. Comput. Phys.*, 1981, vol. 39, pp. 201–25.
8. A. Tomiyama, I. Kataoka, I. Zun, and T. Sakuguchi: *JSME Int J. Ser. B*, 1998, vol. 41, pp. 472–79.
9. I. Zun: *Int. J. Multiph. Flow*, 1980, vol. 6, pp. 583–88.
10. A. Tomiyama, H. Tamai, I. Zun, and S. Hosokawa: *Chem. Eng. Sci.*, 2002, vol. 57, pp. 1849–58.
11. T. Frank, J. Shi, and A. Burns, in *3rd International Symposium on Two-Phase Flow Modelling and Experimentation*, Pisa, 2004.
12. R.M. Wellek, A.K. Agrawal, and A.H.P. Skelland: *AIChE J.*, 1966, vol. 12, pp. 854–62.
13. M.T. Dhotre, N.G. Deen, B. Niceno, Z. Khan, and J.B. Joshi: *Int. J. Chem. Eng.*, 2013, vol. 64, 343276.
14. J. Smagorinsky: *Mon. Weather Rev.*, 1963, vol. 91, pp. 99–164.
15. J.W. Deardorff: *J. Fluid Mech.*, 1970, vol. 41, pp. 453–80.
16. B. Ničeno, M.T. Dhotre, and N.G. Deen: *Chem. Eng. Sci.*, 2008, vol. 63, pp. 3923–31.
17. R. Sungkorn, J.J. Derksen, and J.G. Khinast: *Chem. Eng. Sci.*, 2011, vol. 66, pp. 2745–57.
18. M. Milelli, B.L. Smith, and D. Lakehal: in *Direct and Large-Eddy Simulation IV*, Springer, 2001, pp. 461–70.
19. E Delnoij, FA Lammers, J.A.M. Kuipers, and W.P.M. van Swaaij: *Chem. Eng. Sci.*, 1997, vol. 52, pp. 1429–58.
20. N.G. Deen, M. van Sint Annaland, and J.A.M. Kuipers: *Chem. Eng. Sci.*, 2004, vol. 59, pp. 1853–61.
21. G. Hu and I Celik: *Chem. Eng. Sci.*, 2008, vol. 63, pp. 253–71.
22. R. Sungkorn, J.J. Derksen, and J.G. Khinast: *AIChE J.*, 2012, vol. 58, pp. 1356–70.
23. B Fraga, T Stoesser, CCK Lai, and SA Socolofsky: *Ocean Model.*, 2016, vol. 97, pp. 27–36.
24. T. Haas, C. Schubert, M. Eickhoff, and H. Pfeifer: *Chem. Eng. Sci.*, 2020.
25. T. Ziegenhein, A. Tomiyama, and D. Lucas: *Int. J. Multiph. Flow*, 2018, vol. 108, pp. 11–24.
26. Y.Y. Sheng and G.A. Irons: *Metall. Trans. B*, 1993, vol. 24, pp. 695–705.
27. M.B. Goldschmit and A.H. Coppola Owen: *Ironmak. Steelmak.*, 2001, vol. 28, pp. 337–41.
28. Y.Y. Sheng and G.A. Irons: *Metall. Mater. Trans. B*, 1995, vol. 26, pp. 625–35.
29. C.G. Méndez, N. Nigro, and A. Cardona: *J. Mater. Process. Technol.*, 2005, vol. 160, pp. 296–305.
30. H. Duan, Y. Ren, and L. Zhang: *JOM*, 2018, vol. 70, pp. 2128–38.
31. W. Lou and M. Zhu: *Metall. Mater. Trans. B*, 2013, vol. 44, pp. 1251–63.
32. D. Pfleger and S. Becker: *Chem. Eng. Sci.*, 2001, vol. 56, pp. 1737–47.
33. T. Ma, C. Santarelli, T. Ziegenhein, D. Lucas, and J. Fröhlich: *Phys. Rev. Fluids*, 2017, vol. 2, p. 034301.
34. M. Kraume and P. Zehner: *Chemie Ingenieur Technik*, 1989, vol. 61, pp. 332–33.
35. Y. Xie, S. Orsten, and F. Oeters: *ISIJ Int.*, 1992, vol. 32, pp. 66–75.
36. M. Sano and K. Mori: *Trans. Jpn. Inst. Met.*, 1976, vol. 17, pp. 344–52.
37. B. Trummer, W. Fellner, A. Viertauer, L. Kneis, and G. Hackl: *RHI Bull.*, 2016, vol. 1, p. 35–38.
38. K.B. Owusu, T. Haas, P. Gajjar, M. Eickhoff, P. Kowitwarangkul, and H. Pfeifer: *Steel Res. Int.*, 2019, vol. 90, p. 1800346.
39. P. Gajjar, T. Haas, K.B. Owusu, M. Eickhoff, P. Kowitwarangkul, and H. Pfeifer: *Eng. Sci. Technol.*, 2019, vol. 22, pp. 538–547.
40. D. Lucas, H.-M. Prasser, and A. Manera: *Chem. Eng. Sci.*, 2005, vol. 60, pp. 3609–619.
41. T.R. Auton: *J. Fluid Mech.*, 1987, vol. 183, pp. 199–218.
42. R. Adoua, D. Legendre, and J. Magnaudet: *J. Fluid Mech.*, 2009, vol. 628, pp. 23–41.
43. S. Aoyama, K. Hayashi, S. Hosokawa, D. Lucas, and A. Tomiyama: *Int. J. Multiph. Flow*, 2017, vol. 96, pp. 113–22.
44. W. Dijkhuizen, M. van Sint Annaland, and JAM Kuipers: *Chem. Eng. Sci.*, 2010, vol. 65, pp. 1274–87.
45. D. Legendre and J. Magnaudet: *J. Fluid Mech.*, 1998, vol. 368, pp. 81–126.
46. G. Bozzano and M. Dente: *Comput. Chem. Eng.*, 2001, vol. 25, pp. 571–76.
47. W. Dijkhuizen, I. Roghair, M. van Sint Annaland, and JAM Kuipers: *Chem. Eng. Sci.*, 2010, vol. 65, pp. 1415–26.
48. R. Mei and J.F. Klausner: *Phys. Fluids A Fluid Dyn.*, 1992, vol. 4, pp. 63–70.
49. I Roghair, YM Lau, NG Deen, HM Slagter, MW Baltussen, M Van Sint Annaland, and JAM Kuipers: *Chem. Eng. Sci.*, 2011, vol. 66, pp. 3204–211.
50. D. Bröder and M. Sommerfeld: *Meas. Sci. Technol.*, 2007, vol. 18, pp. 2513–28.
51. D.K. Lilly: *Phys. Fluids A Dyn.*, 1992, vol. 4, pp. 633–35.
52. W.-W. Kim,and S. Menon: in *35th Aerospace Sciences Meeting and Exhibit*, 1997, p. 210.